On the Accuracy of Landweber and Tikhonov Reconstruction Techniques in Gas-Solid Fluidized Bed Applications

M. Banaei, M. van Sint Annaland, J. A. M Kuipers, and N. G. Deen
Dept. of Chemical Engineering and Chemistry, Multiphase Reactors Group, Eindhoven University of Technology, 5600 MB Eindhoven, The Netherlands

DOI 10.1002/aic.14976
Published online August 11, 2015 in Wiley Online Library (wileyonlinelibrary.com)

As electrical capacitance tomography technique needs a sophisticated reconstruction, the accuracy of two of the most widely used reconstruction techniques (Landweber and Tikhonov) for gas-fluidized bed applications were assessed. For this purpose, the results of two-fluid model simulations were used as an input of reconstruction. After finding the optimum reconstruction parameters for the studied system, it is found that both techniques were able to obtain the radial profile and overall value of average volume fraction very well. Conversely, both methods were incapable to determine bubble sizes accurately especially small bubble sizes, unless the Landweber technique with inverted Maxwell concentration model is applied. The probability distribution of the reconstructed results was also smoother in transition between the emulsion and bubble phases compared to the reality. Finally, no significant differences in noise immunity of these two techniques were observed. © 2015 American Institute of Chemical Engineers *AIChE J*, 61: 4102–4113, 2015
Keywords: gas-solid fluidized bed, electrical capacitance tomography, two-fluid model, Landweber and Tikhonov reconstruction, accuracy analysis

Introduction

Gas fluidized beds are one of the most important gas-solid contactors and are widely used in the process industries. Polymerization, drying, and granulation are a few examples of their applications.[1–6] Due to the importance of these contactors, a wide range of experimental techniques has become available to capture their hydrodynamic behavior.[7–15] Each experimental technique has its own advantages and disadvantages. In general, all the experimental techniques can be classified into two categories: intrusive and nonintrusive. Electrical Capacitance Tomography (ECT) is one of the nonintrusive techniques which enable us to obtain a better understanding of fluidization behavior without any disturbance in the fluidized bed. This technique has been widely used by different researchers for different fluidization regimes[16–18] and different bed dimensions and gemoetries.[15,19] In this technique E electrodes are placed around the bed. A certain potential difference is applied to one of the electrodes and the other electrodes are used as detectors. In this way, $E(E-1)/2$ pair interelectrode capacitances can be measured. By considering the governing equations of an ECT system, the measured capacitances can be converted into a spatial permittivity distribution. This is usually done using a sensitivity matrix concept. The spatial permittivity distribution can subsequently be converted to a spatial distribution of the solids volume fraction. However, concentration models are required for this conversion process. As the number of pair interelectrode capacitances are relatively low, the spatial resolution of the final results will be relatively low too (i.e., in comparison with X-ray tomography).

As mentioned earlier, a sensitivity matrix concept can be used for converting the capacitances into permittivity distribution. The sensitivity matrix is a matrix that shows how pair interelectrode capacitances C change when a change is applied in the dielectric constant K of each spatial element: $C = S \cdot K$. In this relation, C is a vector that contains the pair interelectrode capacitances, K is a vector that contains the permittivity of spatial elements, and S is the sensitivity matrix. After measuring the pair interelectrode capacitances, they should be converted to a permittivity distribution by $K = S^{-1} \cdot C$. where S is the sensitivity matrix, K is the permittivity distribution, and C in the pair interelectrode capacitance data. As the sensitivity matrix is a nonsquare matrix, it does not have an inverse. Different reconstruction techniques can be used for solving such an inverse problem. Two of the most important reconstruction techniques are the Landweber[20] and Tikhonov[21] methods. In this work, an attempt was made to find out the optimum values for the parameters used in these techniques when applied to a cylindrical bubbling fluidized bed. After introducing a systematic procedure for finding the optimum parameters, the most suitable parameters were obtained. Then, the accuracy of these techniques in obtaining the overall gas (solids) volume fraction, bubble sizes, the radial solids volume fraction profile and the probability distribution function (PDF) of the gas volume fraction was investigated. This investigation will provide a clearer view on the reliability of ECT results obtained for the aforementioned key hydrodynamic parameters of fluidized bed applications. It will also show the importance of reconstruction parameters on the accuracy of final results.

Correspondence concerning this article should be addressed to N. G. Deen at N.G.Deen@tue.nl.

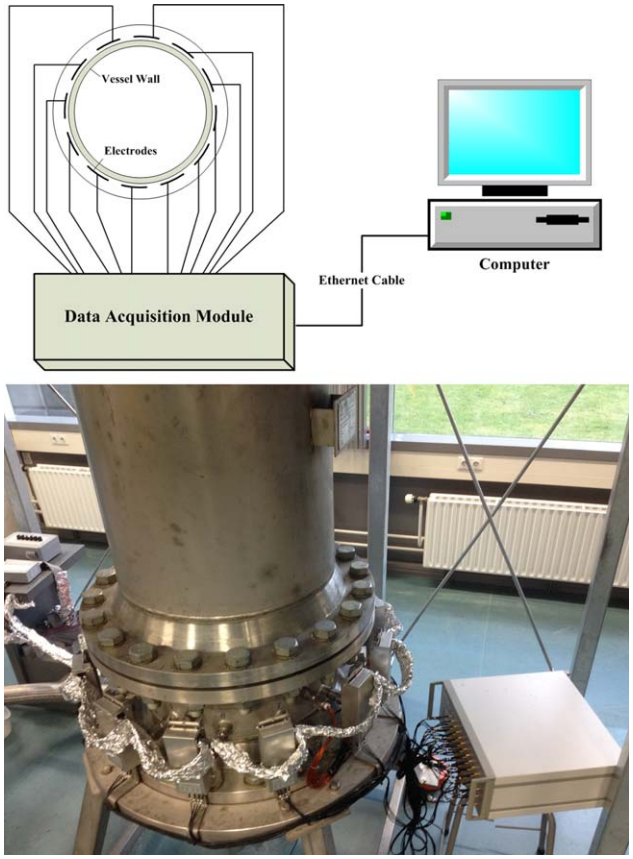

Figure 1. Schematic representation and a picture of ECT facility.

[Color figure can be viewed in the online issue, which is available at wileyonlinelibrary.com.]

Experimental Setup

In this work, 812 spatial elements were used for a system with 12 electrodes. The latter gives 66 independent pair interelectrode capacitances, which is much lower than 812. In other word, C is a vector with 66 elements. K is a vector with the size of 812 and S or the sensitivity matrix has a size of 66 by 812. The experimental setup that has been used in this work was a cylindrical bubbling fluidized bed with 30 cm diameter and ~2 m height. All the electrodes which are placed around the bed have 5 cm height and they have been embedded at 5 different heights which enable us for measurements at different axial positions. Figure 1 presents a schematic image of ECT facility and a picture of the setup. As it can be seen in this figure, all the measured data should be transferred from electrodes to data acquisition module unit. After that, the data is transferred to a computer for reconstruction. For further information about the experimental setup an interested reader can refer to the work by Godlieb et al.[22] It should be also added that the focus of this work is only on the reconstruction part of the results which is the last step of measurements.

Reconstruction Techniques

In this section, a brief description of the mathematical details of the Landweber and Tikhonov reconstruction techniques is given.

Landweber reconstruction

The Landweber reconstruction method is based on a singular value decomposition of the sensitivity matrix. In the first step, the sensitivity matrix is decomposed into three matrices U, D, and V

$$S = U \cdot D \cdot V \tag{1}$$

where U and V are unitary matrices and D is a diagonal matrix. For mathematical details of this decomposition, the interested reader is referred to mathematical text books.[23]

An approximate inverse of the sensitivity matrix (S_L) can be obtained using U, V, and a filter matrix (F)

$$S_L = V \cdot F \cdot U^T \tag{2}$$

The elements of the filter matrix F can be obtained from

$$f = (1 - L \cdot d)^N / d \tag{3}$$

In this equation, d is a diagonal element of D, L is the relaxation parameter (or Landweber transformation parameter), and

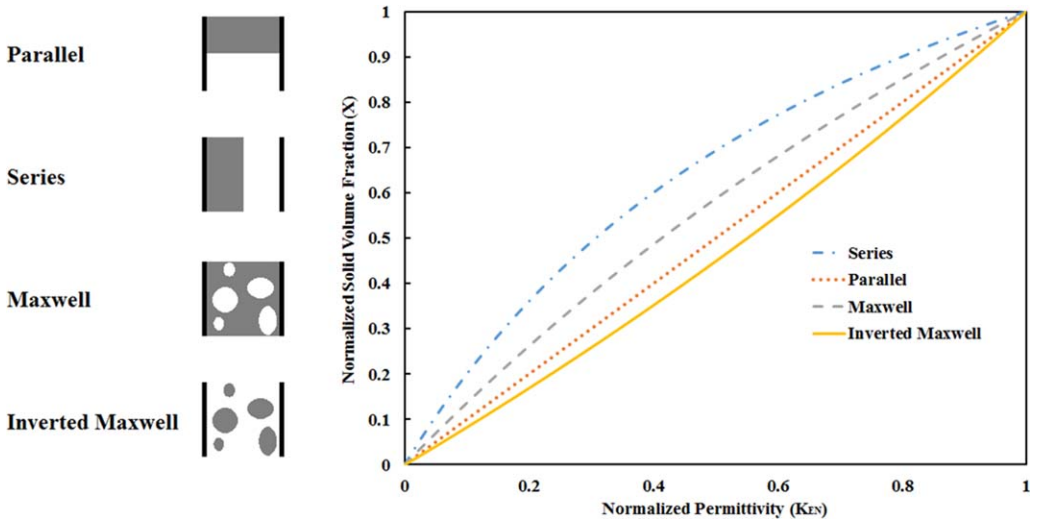

Figure 2. Schematic representation of concentration models for conversion of the measured normalized permittivity to phase volume fraction.

[Color figure can be viewed in the online issue, which is available at wileyonlinelibrary.com.]

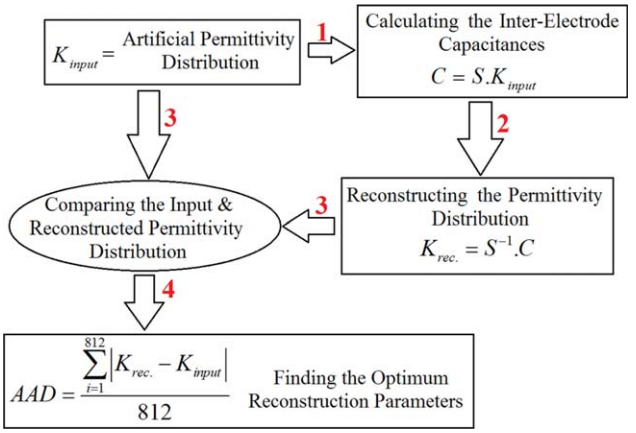

Figure 3. Schematic representation of the procedure for determination of accuracy and optimum parameters of reconstruction techniques.

[Color figure can be viewed in the online issue, which is available at wileyonlinelibrary.com.]

N is the Landweber constant. After calculation of S_L, it is possible to obtain the permittivity distribution by

$$K = S_L \cdot C \tag{4}$$

Tikhonov reconstruction

The Tikhonov reconstruction technique was proposed by Tikhonov and Arsenin[24] in 1977. In this technique, the back projected permittivity is calculated by

$$K_{BP} = S^T \cdot C \tag{5}$$

In the back projection method, it is assumed that the inverse of the sensitivity matrix is equal to its transpose. As $C = S \cdot K$, we may write

$$K = (S^T \cdot S)^{-1} \cdot K_{BP} \tag{6}$$

By substituting Eq. 5 into Eq. 6, we obtain

$$K = (S^T \cdot S)^{-1} \cdot S^T \cdot C \tag{7}$$

The matrix $(S^T \cdot S)^{-1}$ can have a very small elements appearing on its diagonal. To prevent singularity in the final results, an additional term is introduced which leads to Eq. 8

$$K = (S^T \cdot S + t \cdot I)^{-1} \cdot S^T \cdot C \tag{8}$$

where t is a scalar value which is called the Tikhonov constant and I is the identity matrix.

Concentration Models

Concentration models are used to convert the permittivity distribution into volume fraction data. Series, parallel, Maxwell and inverted Maxwell are some of the most frequently

Table 1. Input (Ground) Case Description

	$D_{bub.}/D_{bed}$	Bubble's Location
Test Case a1	0.1216	Center of the Bed
Test Case a2	0.2531	Center of the Bed
Test Case a3	0.3059	Center of the Bed
Test Case a4	0.4494	Center of the Bed
Test Case a5	0.3059	Near to Wall Boundaries

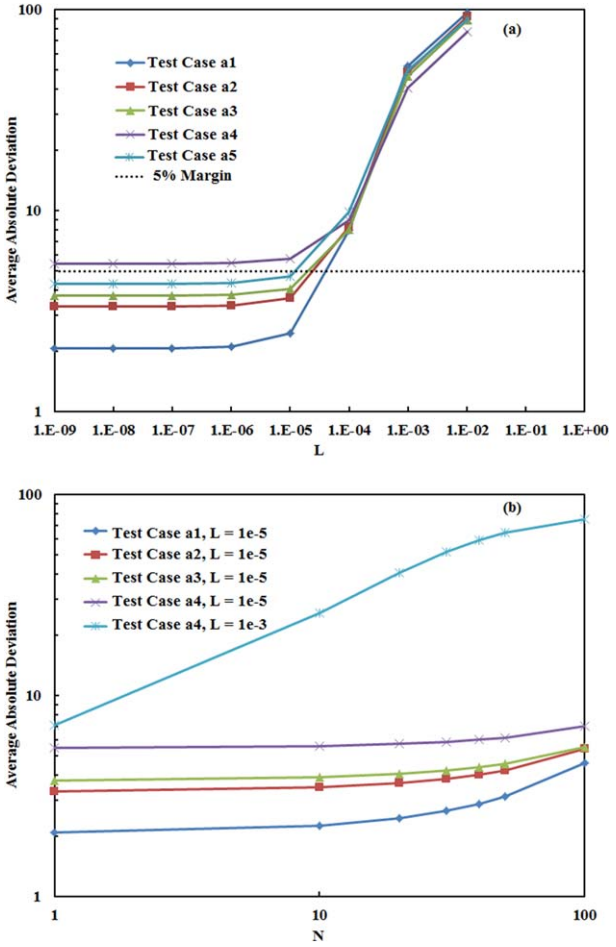

Figure 4. Average absolute deviation of the reconstructed normalized permittivity distribution as a function of (a) the relaxation parameter L (for $N = 20$) and (b) the Landweber constant N (for $L = 10^{-3}$ or 10^{-5}).

[Color figure can be viewed in the online issue, which is available at wileyonlinelibrary.com.]

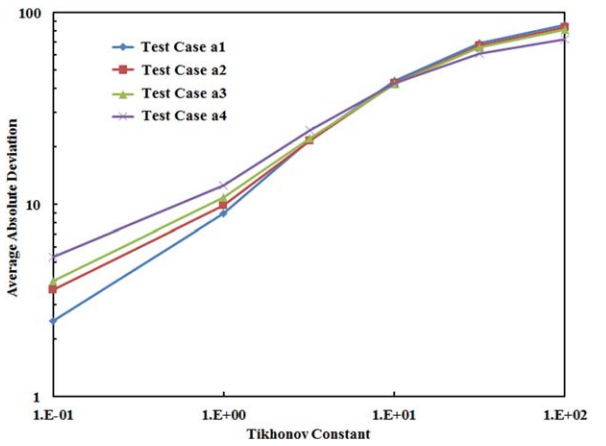

Figure 5. Average absolute deviation of the reconstructed normalized permittivity distribution as a function of the Tikhonov constant t.

Tikhonov constants smaller than 0.1 could lead to singularity issues and were not used in the test cases. [Color figure can be viewed in the online issue, which is available at wileyonlinelibrary.com.]

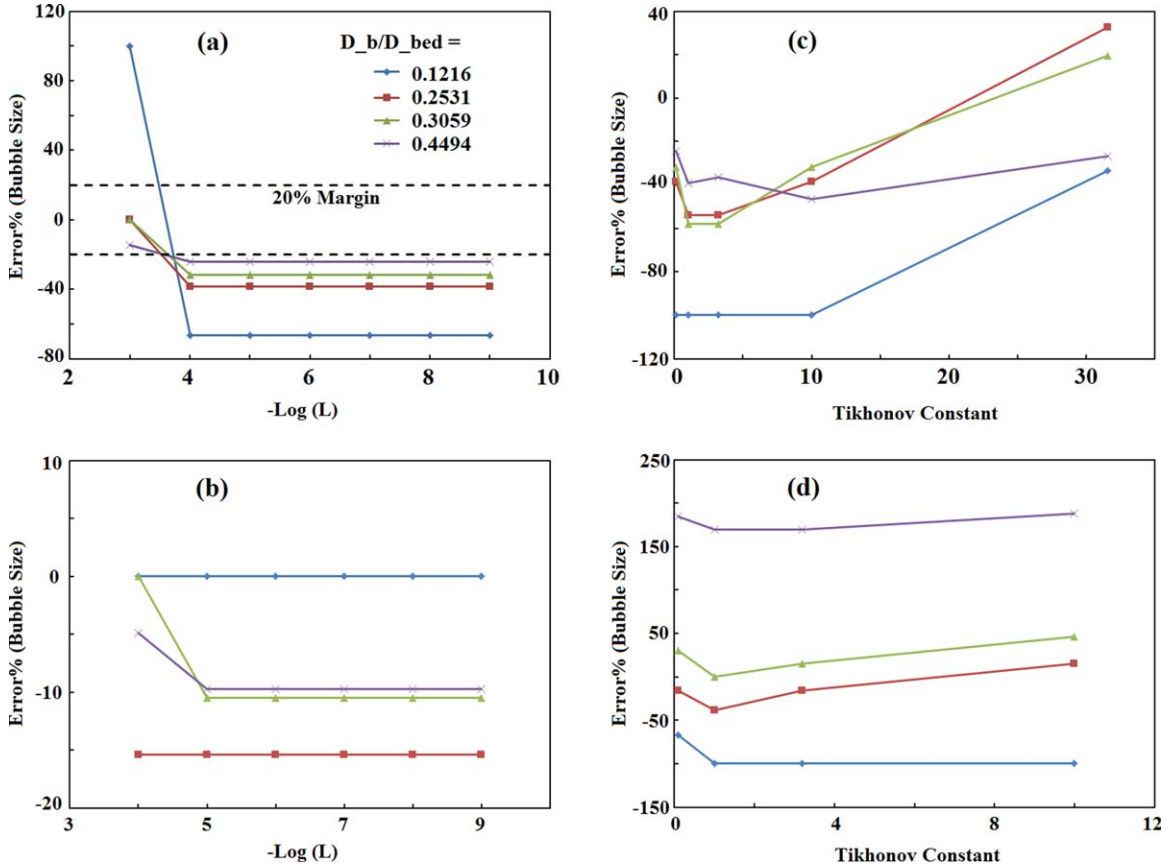

Figure 6. Sensitivity of the reconstructed bubble diameter to (a) the Landweber relaxation parameter (Landweber constant $N = 20$), using the series concentration model, (b) the Landweber relaxation parameter (Landweber constant $N = 20$), using the inverted Maxwell concentration model, (c) the Tikhonov constant, using series concentration model, and (d) the Tikhonov constant, using Inverted Maxwell concentration model.

[Color figure can be viewed in the online issue, which is available at wileyonlinelibrary.com.]

used models. Equations 9–12 give the expressions for these models which are obtained on basis of the calculation of a mixture permittivity in series, parallel, Maxwellian and inverted Maxwellian configurations of two dielectric material. The schematic representation of these concentration models is shown in Figure 2. For more information and details, the interested reader is referred to the study of Godlieb[25]

$$X = \frac{K_r.K_{EN}}{1+K_{EN}(K_r-1)} \quad \text{Series Model} \tag{9}$$

$$X = K_{EN} \quad \text{Parallel Model} \tag{10}$$

$$X = \frac{K_{EN}(2+K_r)}{3+K_{EN}(K_r-1)} \quad \text{Maxwell Model} \tag{11}$$

$$X = \frac{2K_{EN}K_r+K_{EN}}{3K_r+K_{EN}-K_{EN}K_r} \quad \text{Inverted Maxwell Model} \tag{12}$$

In these equations X is the normalized solid volume fraction $(\varepsilon_s = \varepsilon_{s,max}.X)$, K_r is the permittivity ratio of the materials in the bed (higher permittivity to lower permittivity) and K_{EN} is the normalized permittivity. In this work, $\varepsilon_{s,max}$ or maximum solid packing of 0.63 was used. The normalized permittivity can be simply calculated by $K_{EN} = \frac{K-K_{low}}{K_{high}-K_{low}}$ where K_{low} is the lowest possible permittivity in the bed (when the bed is completely empty) and K_{high} is the highest possible permittivity in the bed (when the bed is filled with particles but it is not fluidized yet). The calibration of the setup is also done based on the highest and lowest possible permittivity distribution in the bed. When the setup is completely empty, the pair interelectrode capacitances should be measured. After that, the setup should be filled with particles and the pair interelectrode capacitances should be measured again. In this way, it is possible to determine the permittivity distribution after any measurements in the bed by the aid of these two lower and upper limits.

Results and Discussions

Optimum reconstruction parameter

In this section, a systematic procedure for determination of the optimum reconstruction parameters is presented. This method contains couple of steps. Figure 3 presents the whole procedure in a schematic way. In this method, an artificial permittivity distribution (K_{in}) was created from a bubble placed in a plane filled with particles. After that, the pair interelectrode capacitances were calculated by $C = S \cdot K_{in}$. Subsequently, a reconstructed distribution (K_{rec}) was calculated by $K_{rec} = S^{-1} \cdot C$ and compared with the input values of the permittivity distribution. Different test cases were conducted and the final results were compared to their corresponding input case. This process was done with different reconstruction

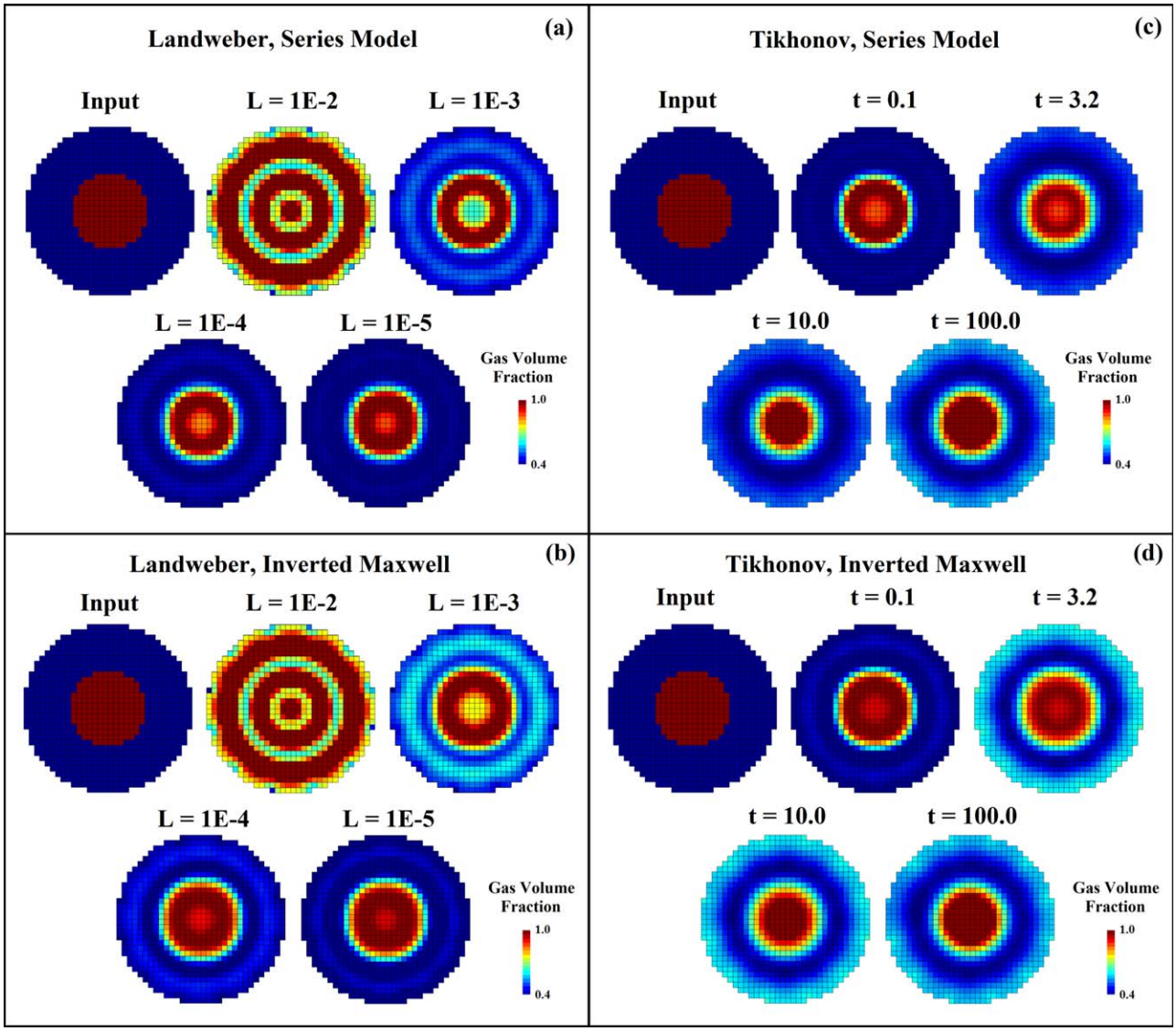

Figure 7. Effect of (a, b) Landweber relaxation parameter on the reconstruction result ($N = 20$) and (c, d) Tikhonov constant on the reconstruction results.

[Color figure can be viewed in the online issue, which is available at wileyonlinelibrary.com.]

parameters. In this way, the optimum parameters for Landweber and Tikhonov techniques can be obtained.

In the first series of input (ground) cases, one bubble was located inside the measurement plane in the bed. Different bubble diameters were chosen and the accuracy of the results was quantified on basis of the average absolute deviation (AAD) of the permittivity in all the 812 spatial elements

$$\mathrm{AAD} = \frac{1}{812}\sum_{i=1}^{812}|K_{\mathrm{rec.}} - K_{\mathrm{input}}| \tag{13}$$

Table 1 shows the test case descriptions. In all of these five test cases, the permittivity distribution was normalized before reconstruction. In other words, the normalized permittivity of the bubble phase is zero and for the emulsion it is one.

Figures 4 and 5 show the results obtained from all test cases using different reconstruction parameters.

In test case a5 (where the bubble was located near to the bed boundary), the AAD was slightly larger than its corresponding value in test case a3 (where a bubble of the same size was located in the center). As can be seen from Figure 4, the accuracy decreases with increasing Landweber constant and increasing value of the relaxation parameter. In the case that the relaxation parameter was smaller than 10^{-5}, the AAD was less than 10% and the Landweber constant did not have a significant impact on the final results of these test cases. The Landweber constant could change the accuracy significantly if a large relaxation parameter like 10^{-3} was used (refer to Figure 4b). For such cases, the AAD increased with increasing the value of Landweber constant. This observation can be justified by the semiconvergence behavior of ill-posed problems.[26] It can be concluded that a relaxation parameter less than 10^{-5} with an arbitrary Landweber constant between 1 and 20 are suitable parameters in the Landweber reconstruction method for the studied system.

Figure 5 represents the obtained AAD depending on the Tikhonov constant. As can be seen from this figure, $t = 0.1$ is the optimum parameter in all the test cases. This parameter gave less than 10% AAD for the final reconstructed normalized permittivity. It was also observed that the AAD increases

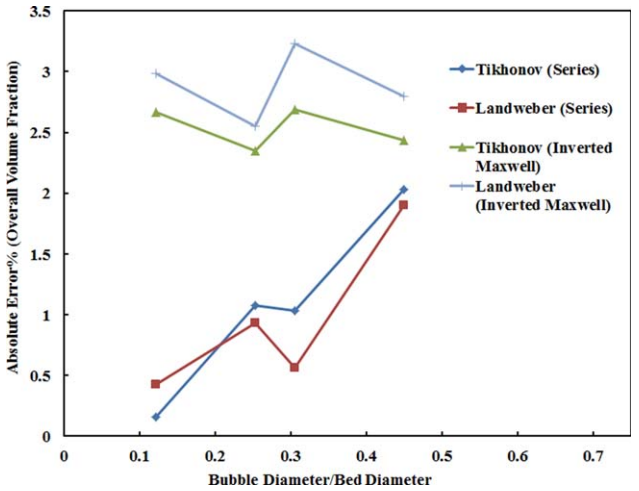

Figure 8. Accuracy of reconstruction techniques for overall volume fraction, $L = 10^{-5}$, $N = 20$ was used in the Landweber technique and $t = 0.1$ was used as Tikhonov constant.

[Color figure can be viewed in the online issue, which is available at wileyonlinelibrary.com.]

with increased bubble size regardless of the reconstruction technique, even though the average permittivity becomes smaller. As the elements in the main diagonal of $S^{T} \cdot S$ can be very small or even zero, Tikhonov constants smaller than 0.1 can lead to singularity. Therefore, all the Tikhonov constants that are used in the test cases were equal to or larger than 0.1.

Accuracy evaluation of reconstruction techniques

In this section, the accuracy of the two reconstruction techniques for measuring four different key parameters in gas-fluidized beds is presented. These parameters are the overall volume fraction, the bubble size, the radial profile of the volume fraction, and the PDF of the volume fraction.

Bubble Detection Accuracy. Test cases a1–a4 were performed once again with different reconstruction parameters. The solids volume fraction $\varepsilon_s = 0.6$ was assumed in the emulsion phase and the bubble phase was considered completely free of solid phase ($\varepsilon_s = 0$). A gas volume fraction $\varepsilon_{g,th} = 0.8$ was used as a threshold for bubble phase detection, that is, spatial elements with $\varepsilon_g > \varepsilon_{g,th}$ were considered to be inside a bubble. Figures 6a, b present the effect of the Landweber relaxation parameter on the accuracy of the bubble size determination.

Figure 6a shows the reconstruction results obtained with the series concentration model. In this case, when a relaxation parameter smaller than 10^{-4} was used, the relative error in detecting the diameter of large bubbles was smaller than for small bubbles. The optimum relaxation parameter for the bubble size was obtained between 10^{-3} and 10^{-4} for $D_{bub}/D_{bed} = 0.1216$ and it increased to a number between 10^{-2} and 10^{-3} for $D_{bub}/D_{bed} = 0.4494$. There was a sudden change in the results after increasing the value of relaxation parameter beyond 10^{-3} (not shown in Figure 6). It was also observed that for small bubbles like $D_{bub}/D_{bed} = 0.1216$ and a relaxation parameter smaller than 10^{-5} the error was around -60%. It clearly shows the inability of the Landweber reconstruction technique for small bubble detection. Note that the Landweber constant N did not have any effect on the bubble size for $L = 10^{-5}$.

As series and inverted Maxwell concentration models are the upper and lower limits for solid volume fraction determination (refer to Figure 2), only the effect of these two concentration models were investigated in this work. Figure 6b presents the reconstruction results this time obtained with the inverted Maxwell concentration model. With this concentration model, the results for bubble detection were improved considerably, especially for small bubbles. It is also found that except the results of case a1, the trends in the error are similar to the results obtained with the series concentration model. In this situation the best results were obtained with a relaxation parameter smaller than $10^{-4}-10^{-5}$. A sudden increase in the bubble size error around $L = 10^{-3}$ was also observed. Some snapshots of the reconstructed results are presented in Figure 7 to illustrate this effect more clearly.

Figure 7a presents some snapshots of reconstructed images obtained with Landweber and series concentration model for different relaxation parameters. As can be seen from this figure, even though the error for $L = 10^{-3}$ is smaller than for $L = 10^{-4}$ or $L = 10^{-5}$, inside the bubble the reconstruction fails, as it gives very different values as compared to the input. For the case with $L = 10^{-3}$, a gas volume fraction gradient was observed in the bubble region but all the cells inside of the bubble still had a gas fraction exceeding 0.8. For relaxation parameter of $L = 10^{-2}$, the results were completely different from the input case. It can also be seen that with a relaxation parameter smaller than $L = 10^{-4}$, the bubble size is under-predicted in all the observed cases. This figure also shows that with small relaxation parameters like 10^{-5}, the volume fraction exterior to the bubble can be reconstructed very well but the bubble-emulsion boundaries cannot be reconstructed so well.

Snapshots of the same results obtained with the inverted Maxwell model are also presented in Figure 7b. Similar to Figure 7a, the bubble edges could not be detected very well, regardless of the value of the relaxation parameter. Smaller relaxation parameters lead to higher accuracy outside the bubble phase. The optimum parameter value was around $10^{-4}-10^{-5}$. The results with a relaxation parameter larger than 10^{-3} were completely unreliable.

The same test cases were also conducted applying the Tikhonov technique. The results are presented in Figures 6c, d. This figure clearly shows that this technique is not able to reconstruct small bubbles neither. It can also be observed that with a Tikhonov constant smaller than or equal to 31.6, the bubble size is under-predicted for all the test cases. With a Tikhonov constant of 100, the results are unreliable regardless of the bubble size (not shown). Figures 7c, d present some snapshots illustrating the effect of the Tikhonov constant on the reconstructed volume fractions. This figure clearly shows the unreliability of the results with a Tikhonov constant of 100. However, the error in the bubble size with a Tikhonov constant of 100 was much lower than the error in the bubble size with a Tikhonov constant of 0.1 for some cases. Changing the concentration model from the series to the inverted

Table 2. Simulation's Conditions for Two Fluid Modeling

$\Delta r = 0.005$ (m)	$\Delta t = 2.0\times10^{-5}$ (s)	$u_g = 0.417$ (m/s)
$\Delta z = 0.005$ (m)	$d_p = 0.001$ (m)	$T = 293.0$ (K)
$n_r = 30$	$\rho_p = 850$ (kg/m^3)	$\mu_g = 1.8\times10^{-5}$ (Pa.s)
$n_\theta = 30$	ρ_g calculated by ideal gas law	Bed aspect ratio = 1.0
$n_z = 300$	$D_{bed} = 30.0$ (cm)	$e = 0.60$, $e_w = 0.97$

Drag correlation: van der Hoef et al.[30]
Frictional model: Srivastava and Sundaresan[31]
TVD discretization scheme for convection terms: Min-mod[32]

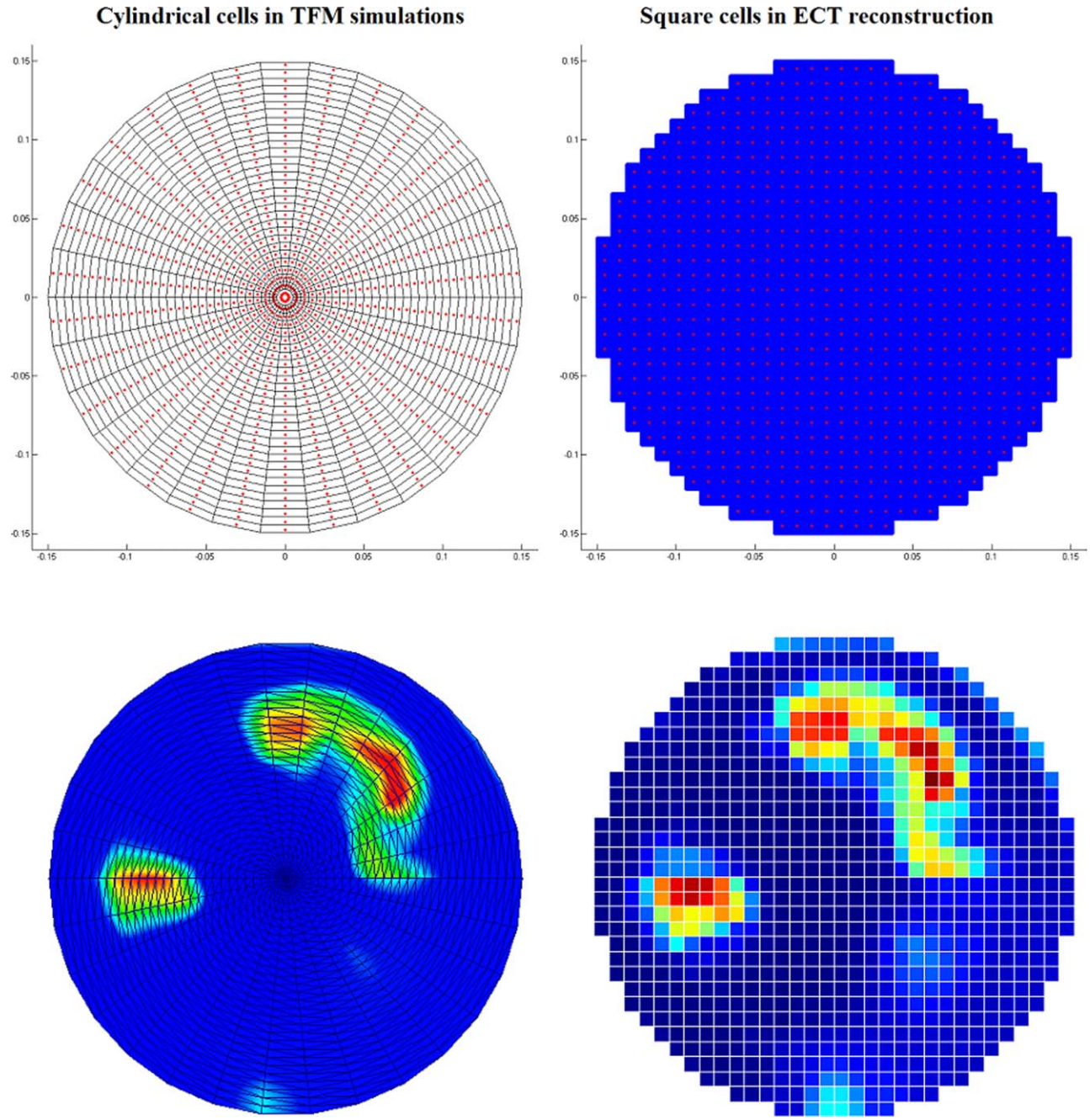

Figure 9. Mapping of TFM simulation results (in cylindrical coordinates) to ECT grid cells (in Cartesian coordinates). Dark blue indicates the normalized permittivity of zero and dark red indicates the normalized permittivity of 1.

[Color figure can be viewed in the online issue, which is available at wileyonlinelibrary.com.]

Maxwell model did not improve the results and even made it worse for some cases.

With consideration of the results for these four test cases, it is concluded that the Landweber technique with inverted Maxwell concentration model, using a relaxation parameter less than $10^{-4}-10^{-5}$ gives the best results for the determination of the bubble size for the studied system. Note that neither of these four test cases (test cases a1–a4), a gradient in the axial direction exists. In another words, bubbles have a cylindrical shape in these test cases. In reality however, the electrodes have a certain height and small bubbles may be covered by emulsion phase to a large extent. In this situation, reconstruction of these bubbles obviously becomes difficult.

Overall Volume Fraction Accuracy. The same test cases were used to determine the accuracy of the reconstructed overall volume fraction. The results showed that the reconstruction techniques with suitable parameters are very accurate in finding the overall volume fraction. Figure 8, shows the absolute error in the overall volume fraction for the test cases a1–a4. As can be observed from this figure, the absolute error was less than 3.5% for all the test cases.

In reality, there will be more than one bubble in a bubbling fluidized bed and the interaction between bubbles will affect the accuracy of the results. The bubble shape is also not completely spherical, which will also change the accuracy of the reconstruction. Note that the ECT results are two-dimensional

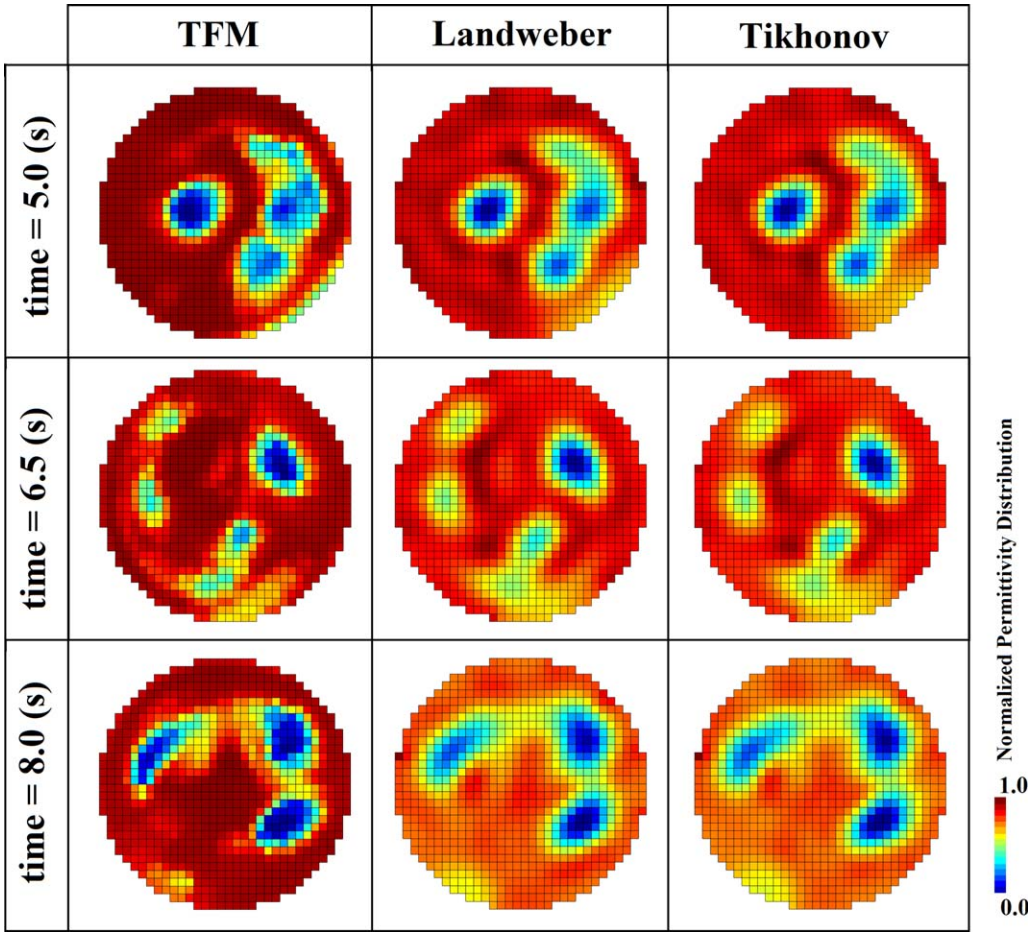

Figure 10. Landweber and Tikhonov reconstruction of TFM results for permittivity distribution at different moments. $L = 10^{-5}$, $N = 1$ was used for Landweber technique and $t = 0.1$ was used as Tikhonov constant.

[Color figure can be viewed in the online issue, which is available at wileyonlinelibrary.com.]

(2-D) projections of the material distribution inside a horizontal slab with a certain thickness ("the measurement plane"). As such, the reconstruction results cannot provide any details of the solids distribution in the axial direction and therefore only provide a quasi-2-D solids distribution. To quantify the consequences of this effect, it was decided to use three-dimensional (3-D) computational fluid dynamics data as an input for the ECT technique to test both reconstruction methods. It should be added that some researchers tried to reconstruct the capacitance measurements data in 3-D by changing the configuration of electrodes[27] or using adaptive sensors[28] but in this work only the reconstruction techniques for conventional ECT facilities is investigated.

A 3-D cylindrical two-fluid simulation was performed for creating input data for the reconstruction. This simulation was performed for a bed with similar size of the experimental bed, 30 cm diameter and 1.5 m height. The computational grids were 5 times of particle diameter in the radial and axial directions. The air at 293 K was used as a fluidizing agent and the particles which were used in these simulations were LLDPE particles with 850 (kg/m^3) density and 1.0 mm diameter. Further information about the simulation's condition like drag correlation, discretization scheme, frictional model, and restitution coefficient is presented at Table 2. For further details regarding the governing equations, the interested reader can refer to the work by Verma et al.[29]

As the height of electrodes is much larger than the height of one computational grid cell, it was necessary to make an average over several cells in the axial direction. After that, the results of the simulations could be used as input for the reconstruction. In this work, it is assumed that the height of the electrodes equals 5 cm. It is also assumed that all the cells with the same radial position have almost the same distance to the electrodes, irrespective of their height. This assumption is fairly good near the center because of the relatively large ratio of the bed diameter to the electrode height. In the next section, the mapping of two-fluid model (TFM) results from the cylindrical coordinate system to the ECT reconstruction cells is presented.

Mapping of TFM Results to ECT Reconstruction Grids. As the simulations with the TFM were performed in a cylindrical coordinate system, it was necessary to map the results from the cylindrical cells to the Cartesian ECT grid cells. ECT grid cells have a square shape. Both type of cells and a typical example of the adapted mapping are illustrated in Figure 9. The most accurate way of mapping is integration over the ECT grids. For this purpose, each ECT grid cell was divided into 30×30 smaller subcells. Subsequently, for each subcell the corresponding volume fraction in the cylindrical grid was determined. Then, for each ECT grid cell, the volume fraction was obtained by averaging the volume fractions of all subcells.

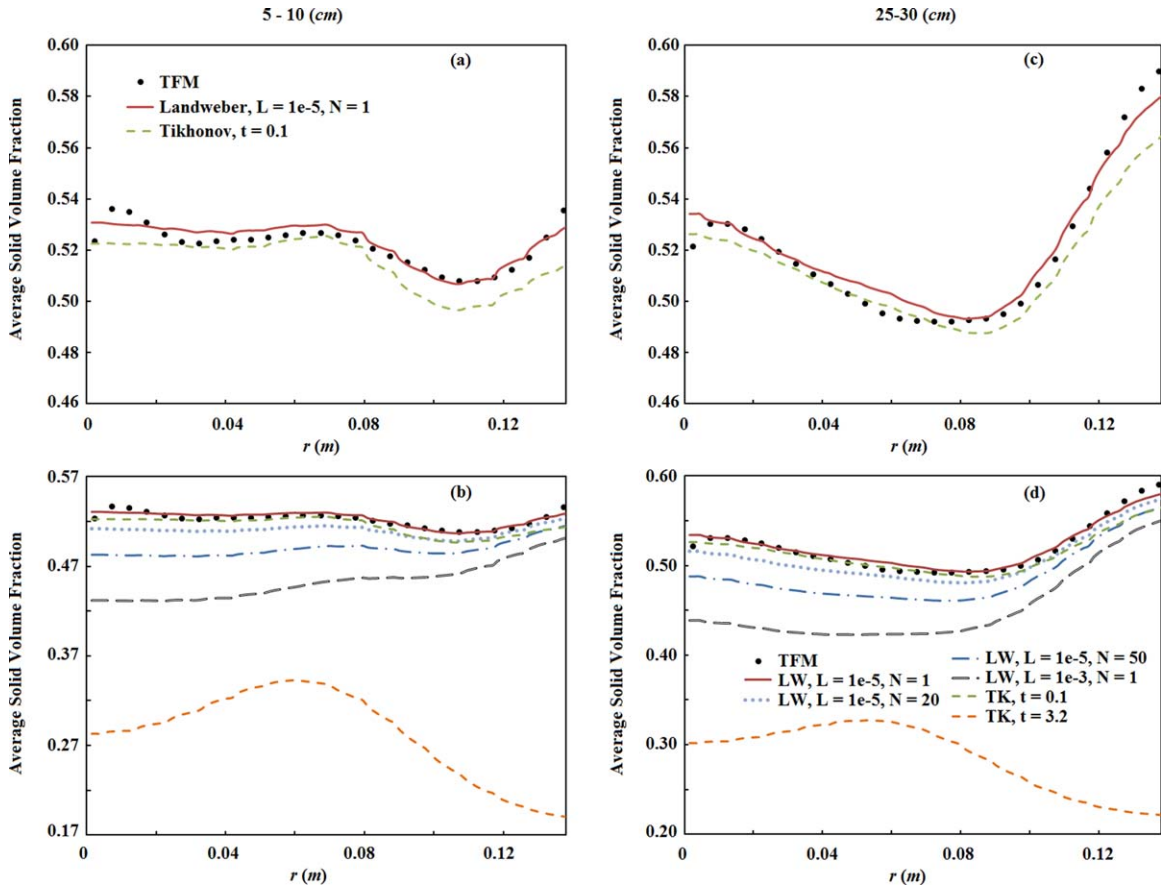

Figure 11. Accuracy of the Landweber and Tikhonov reconstruction techniques with respect to the radial profiles of the average solid volume fraction. LW and TK are abbreviations for Landweber and Tikhonov, respectively.

[Color figure can be viewed in the online issue, which is available at wileyonlinelibrary.com.]

Accuracy of Volume Fraction Radial Profile. After mapping the TFM results to the ECT grid cells, the data was used as an input for the reconstruction techniques. Then, average radial profiles of the solid volume fraction were determined and the results were compared to the results from the input file. This comparison was performed at 5 different heights and the results for $h = 5$–10 cm and $h = 25$–30 cm are presented in Figure 10. It should be added that 9 s of TFM simulation was performed and the last 4 s of simulation was used for processing. Two hundred data files (snapshots) for every seconds of simulation, in total 800 data files, were used in the processing steps. Figure 10 presents some snapshots of Landweber and Tikhonov results for three different moments. Three other aspects should be noted about the processing of the results. All the 800 TFM data files (snapshots) were processed after mapping. In this way, any error arising from the integration is excluded from the analysis. Beside this, the results of the TFM simulations were averaged over 5 cm in the axial direction. In this way, the inability of ECT technique for capturing 3-D information was also excluded from the accuracy analysis of the reconstruction methods. It should be added that parallel concentration model was used for converting TFM data into permittivity distribution and reconstructed permittivity distribution into reconstructed volume fraction (this concentration model was also used for the rest of this work).

Figures 11a, c are the same as Figures 11b, d, respectively. The only difference is that Figures 11a, c only present the accuracy of reconstruction techniques with the most suitable parameters in this system. Figure 11 clearly shows that the Landweber and Tikhonov reconstruction techniques are not only accurate for obtaining the overall average volume fraction but they can also provide the radial profile of solid volume fraction in a very accurate manner if they are used with suitable reconstruction parameters. This accuracy was observed regardless of the bubble size. For example, at height 5–10 cm, the bubbles are much smaller than at 25–30 cm, but the reconstruction results gave good radial profiles for the volume fraction at both heights. Note that the shape of bubbles can also change the accuracy of reconstruction to some extent. It was observed that both reconstruction techniques are less accurate for nonspherical bubbles. Nevertheless, this effect does not significantly affect the results for the average volume fraction profile.

Accuracy of Volume Fraction PDF. As a next step, the accuracy of the Landweber and Tikhonov methods on determining the PDF of the volume fraction is determined. The PDF of the volume fraction was obtained at 5 different heights from the TFM results and they were compared to the reconstructed results. The final results for heights 10–15 and 25–30 cm are presented in Figure 12.

As can be seen from Figures 12c, d, both methods give a shift of the PDF toward higher gas volume fractions as compared to the TFM results. The main reason for this difference is the disability of these two reconstruction methods for detecting regions with high gradients. Both techniques have difficulties to reconstruct the regions with high gradients in the

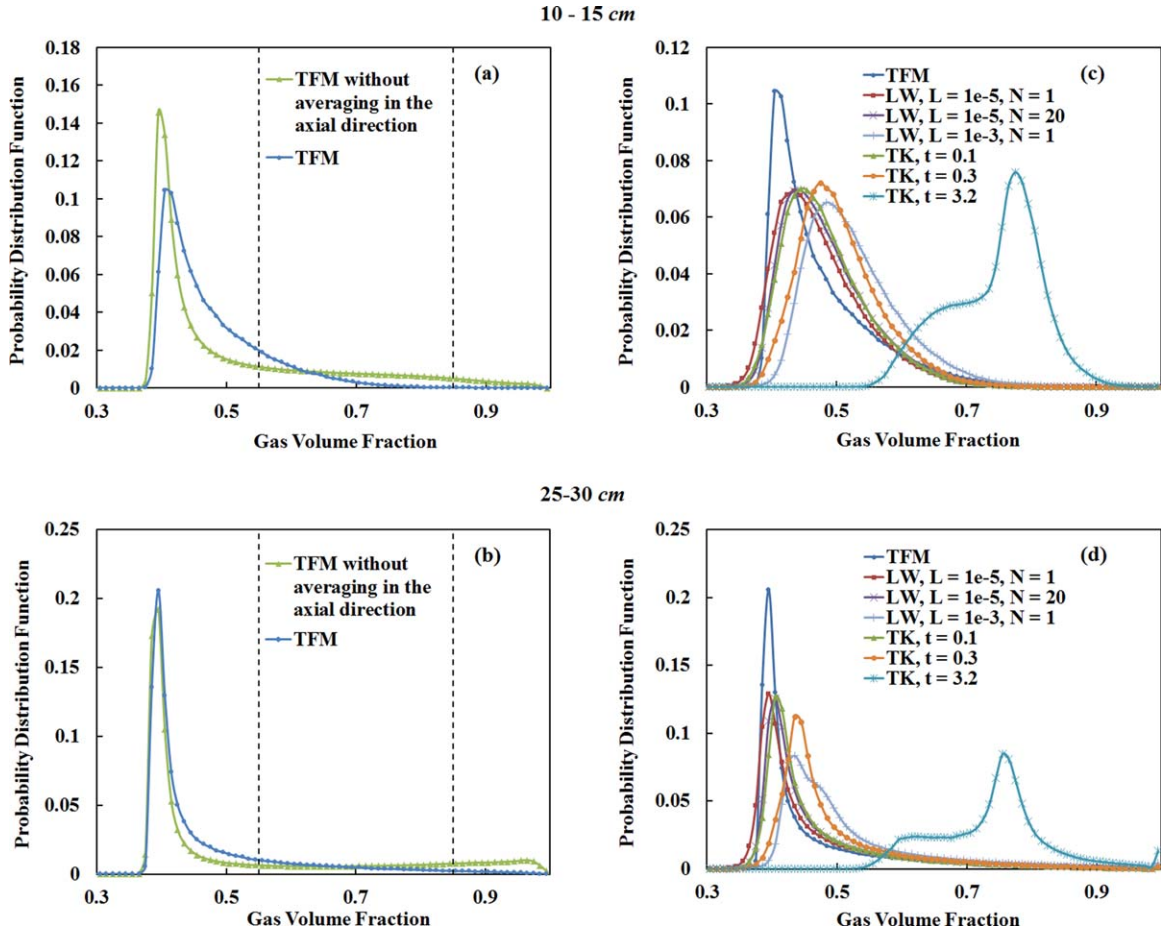

Figure 12. Accuracy of Landweber and Tikhonov methods with respect to the volume fraction PDF. (a) Effect of averaging in the axial direction on PDF at 10–15 cm, (b) effect of averaging in the axial direction on PDF at 25–30 cm, (c) accuracy of Landweber and Tikhonov techniques on PDF at 10–15 cm, and (d) accuracy of Landweber and Tikhonov techniques on PDF at 25–30 cm.

[Color figure can be viewed in the online issue, which is available at wileyonlinelibrary.com.]

volume fraction and consequently the results of the reconstruction are smoother than the TFM results. This can also be observed in Figures 7 and 10. This smoothening causes a less sharp distinction between the reconstructed emulsion and bubble phases which can readily be seen in the PDF.

Figure 12 also shows that Landweber is slightly more accurate than Tikhonov in obtaining the PDF if it is used with suitable parameters. This is in line with the earlier observations for the radial profile of the average volume fraction. It should be noted that the results of the reconstruction are also smoothened by averaging in the axial direction. In Figure 12, the effect of this averaging is shown for the TFM as well (Figures 12a, b). This averaging can lead to a lower probability of both the bubble and emulsion phases and a smoother transition between the two phases. It can be easily seen in Figures 12a, b, that the probability of detecting bubbles decreases considerably after averaging in the axial direction. Figures 11 and 12 both clearly show the importance of systematic determination of optimum reconstruction parameters too. It can be easily seen that the results can change significantly if reconstruction parameters change.

Sensitivity of reconstruction techniques on disturbance

To test the robustness of the reconstruction techniques, test cases a1–a4 have repeated several times (they are repeated for 100 times in this work), but this time with applying a ±5–25% disturbance in the accuracy of the permittivity distribution. In other word, a random noise with the average value of ±5–25% was applied to artificial input permittivity distribution. This noise somehow can mimic the disturbance from environment. In this way, it is possible to find out how different reconstruction techniques respond to these disturbances.

A relaxation parameter of 10^{-5} with $N = 1$ is used for the Landweber reconstruction technique and $t = 0.1$ was used as Tikhonov constant. As can be seen in Figure 13, none of these two techniques has a significant advantage over the other in terms of robustness. It is also observed that, although the AAD increases with bubble size and disturbance percentage, the overall volume fraction can be obtained with typically 90% accuracy. Moreover, one can observe that most of the time the Landweber method gives a slightly lower AAD compared to the Tikhonov method, except for case a4.

Conclusions

In this work, a systematic procedure for determination of optimum parameters for Landweber and Tikhonov reconstruction methods for ECT measurements in gas-fluidized beds is presented. Subsequently, the accuracy of the method for determining key hydrodynamic quantities was investigated for several test cases. These quantities are the overall and radial profile of the average volume fraction, the bubble size and the volume fraction PDF. Finally, the effect of noise on the

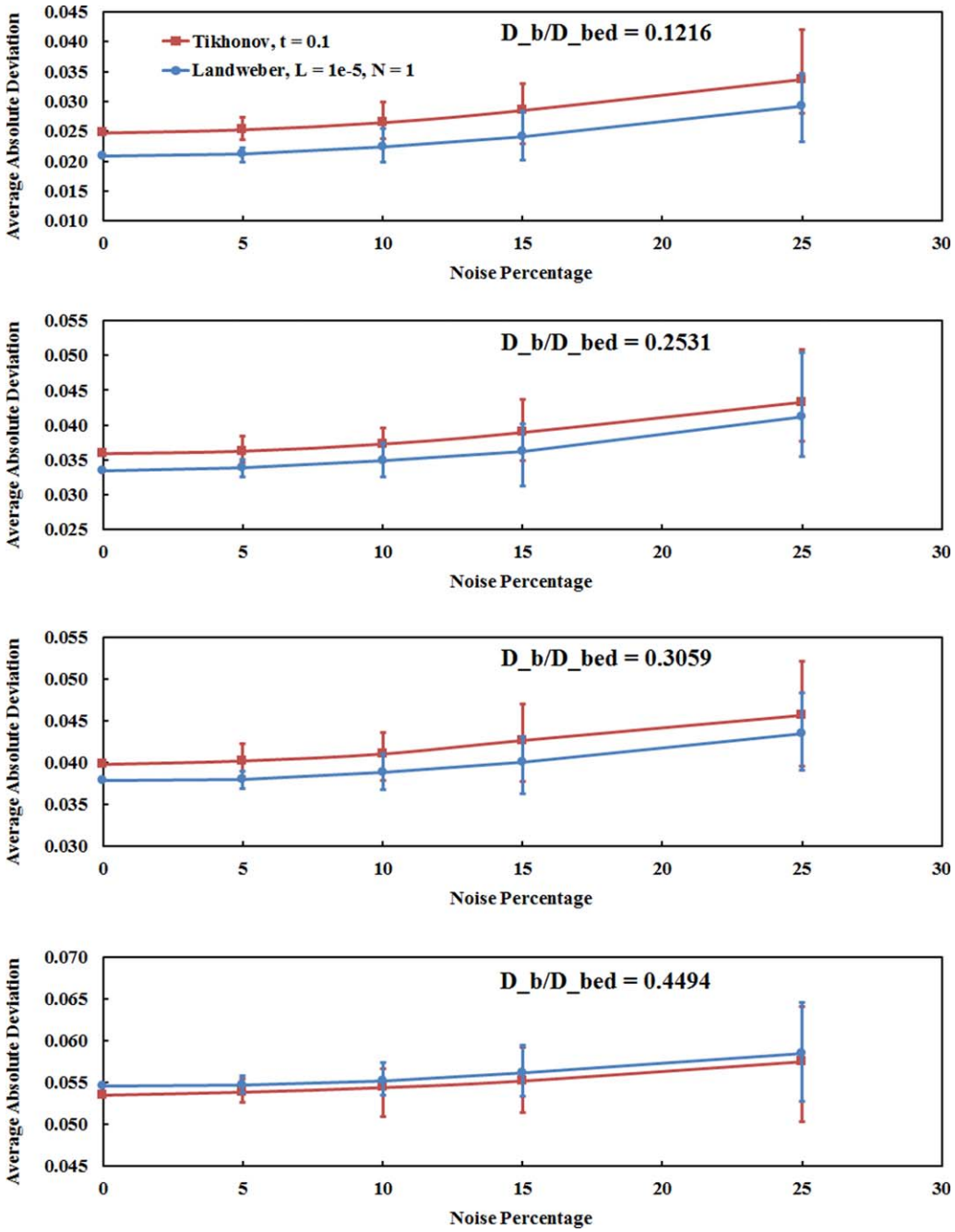

Figure 13. Effect of disturbance on the accuracy of Landweber and Tikhonov reconstruction techniques (the error bars represent the maximum and minimum AAD).

[Color figure can be viewed in the online issue, which is available at wileyonlinelibrary.com.]

performance of the reconstruction techniques was studied as well. Based on this work, it can be concluded as follows:

- It is found that for a cylindrical fluidized bed with 30 cm diameter and 12 electrodes with the height of 5 cm, Landweber relaxation parameter smaller than 10^{-5} with an arbitrary value of the Landweber constant between 1 and 20, and a Tikhonov constant of 0.1–0.3 are the most suitable choices.
- The Tikhonov technique was not able to detect bubble size accurately. This disability is more pronounced for small bubbles.
- The Landweber technique with the series concentration model was also not able to predict the bubble size accurately. The results can be improved significantly when the inverted Maxwell concentration model is used. Note that this conclusion is only valid for cases with zero gradient in the axial direction ("cylindrical bubbles").
- Selection of an improper reconstruction parameter can lead to large errors in the reconstructed volume fractions.
- Both methods provide the overall average gas volume fraction as well as its radial profile very well.
- The probability distribution of the reconstructed results has a smoother transition between emulsion and bubble phases compared to TFM simulation results where typically very large gradients at the bubble-emulsion interface prevail.
- It is found that the two techniques have no significant advantages over each other with respect to noise immunity.

Acknowledgments

This work is part of the Research Programme of Dutch Polymer Institute (DPI) as a project number # 751. The authors also thank Mr. T.T. Hoeben for scientific discussions about this work.

Nomenclature

Roman letters

C = pair interelectrode capacitance
D = diagonal matrix for singular value decomposition process
D_{bed} = bed diameter, m
D_{bub} = bubble diameter, m
d = diagonal elements of D
E = number of electrodes
e = particle–particle restitution coefficient
e_w = particle-wall restitution coefficient
F = filter matrix
h = height from distributor, cm
I = identity matrix
K_{BP} = back-projected permittivity distribution matrix
K_{EN} = normalized permittivity distribution matrix
K_{in} = input permittivity distribution matrix
K_r = permittivity ratio of materials in the bed
K_{rec} = reconstructed permittivity distribution matrix
L = Landweber relaxation parameter
N = Landweber constant
S = sensitivity matrix
S_L = approximate inverse of S by Landweber method
t = Tikhonov constant
U, V = unitary matrices for singular value decomposition process
X = normalized solid volume fraction

Greek letters

ε_g = gas volume fraction
$\varepsilon_{g,th}$ = gas volume fraction threshold for bubble detection
ε_s = solid volume fraction
$\varepsilon_{s,max}$ = maximum solid packing fraction

Abbreviations

AAD = average absolute deviation
BP = back-projected
DAM = data acquisition module
ECT = electrical capacitance tomography
LW = Landweber
TFM = two fluid model
TK = Tikhonov
TVD = total variation diminishing

Literature Cited

1. Link J, Godlieb W, Deen NG, Kuipers JAM. Discrete element study of granulation in a spout-fluidized bed. *Chem Eng Sci*. 2007;62:195–207.
2. Börner M, Hagemeier T, Ganzer G, Peglow M, Tsotsas E. Experimental spray zone characterization in top-spray fluidized bed granulation. *Chem Eng Sci*. 2014;116:317–330.
3. Marandi R, Hashim S, Zahedi G. Hydrodynamic and heat transfer modeling of poly-disperse fluidized bed olefin polymerization reactors. In *22nd ESCAPE, Vol. 30*. 2012:1053–1057.
4. Khan MJH, Hussain MA, Mansourpour Z, Mostoufi N, Ghasem NM, Abdullah EC. CFD simulation of fluidized bed reactors for polyolefin production—a review. *J Ind Eng Chem*. 2014;20:3919–3946.
5. Srinivas G, Pydi Setty Y. Drying behavior of uniform and binary mixture of solids in a batch fluidized bed dryer. *Powder Technol*. 2013;241:181–187.
6. Sharma R, Delebarre A, Alappat B. Chemical-looping combustion—an overview and application of the recirculating fluidized bed reactor for improvement. *Int J Energy Res*. 2014;38:1331–1350.
7. Werther J. Measurement techniques in fluidized beds. *Powder Technol*. 1999;102:15–36.
8. Bartholomew RN, Casagrande RM. Measuring solids concentration in fluidized systems by gamma-ray absorption. *Ind Eng Chem*. 1957;49:428–431.
9. Kruse M, Werther J. 2D gas and solids flow prediction in circulating fluidized beds based on suction probe and pressure profile measurements. *Chem Eng Process: Process Intensification*. 1995;34:185–203.
10. Cheremisinoff NP. Review of experimental methods for studying the hydrodynamics of gas-solid fluidized beds. *Ind Eng Chem Process Des Dev*. 1986;25:329–351.
11. Beck MS. *Tomographic Techniques for Process Design and Operation*. Manchester: Comput. Mech., 1993.
12. Kantzas A, Kalogerakis N. Monitoring the fluidization characteristics of polyolefin resins using X-ray Computer Assisted Tomography scanning. *Chem Eng Sci*. 1996;51:1979–1990.
13. Tsukada M, Ito M, Kamiya H, Horio M. Three-dimension imaging of particle clusters in dilute gas-solid suspension flow. *Can J Chem Eng*. 1997;75:466–470.
14. Bing D, Warsito W, Fan LS. ECT studies of the choking phenomenon in a gas-solid circulating fluidized bed. *AIChE J*. 2004;50:1386–1406.
15. Ge R, Ye J, Wang H, Yang W. Measurement of particle concentration in a Wurster fluidized bed by electrical capacitance tomography sensors. *AIChE J*. 2014;60:4051–4064.
16. Du B, Fan LS, Wei F, Warsito W. Gas and solids mixing in a turbulent fluidized bed. *AIChE J*. 2002;48:1896–1909.
17. Du B, Warsito W, Fan LS. Bed nonhomogenity in turbulent gas-solid fluidization. *AIChE J*. 2003;49:1109–1126.
18. Wang HG, Yang WQ, Senior P, Raghavan RS, Duncan SR. Investigation of batch fluidized-bed drying by mathematical modeling, CFD simulation and ECT measurement. *AIChE J*. 2007;54:427–444.
19. Du B, Warsito W, Fan LS. ECT studies of gas-solid fluidized beds of different diameters. *Ind Eng Chem Res J*. 2005;44:5020–5030.
20. Yang WQ, Spink DM, York TA, McCann H. An image-reconstruction algorithm based on Landweber's iteration method for electrical-capacitance tomography. *Meas Sci Technol*. 1999;10:1065–1069.
21. Yang WQ, Peng L. Image reconstruction algorithms for electrical capacitance tomography. *Meas Sci Technol*. 2003;14:R1–R13.
22. Godlieb W, Gorter S, Deen NG, Kuipers JAM. Experimental study of large scale fluidized beds at elevated pressure. *Ind Eng Chem Res J*. 2012;51:1962–1969.
23. Press WH, Teukolsky SA, Vetterling WT, Flannery BP. *Numerical Recipes: The Art of Scientific Computing*, *3rd ed*. Cambridge: The Cambridge University Press, 2007.
24. Tikhonov VY, Arsenin AN. *Solutions of Ill-Posed Problems*. Washington: AMS, 1977.
25. Godlieb W. *High Pressure Fluidization*, PhD Thesis. Technical University of Twente, Enschede, The Netherlands, 2010.
26. Nikazad T. The use of Landweber Algorithm in Image Reconstruction, PhD Thesis. Linkopings Institute of Technology, Linkoping, Sweden, 2007.
27. Wang F, Marashdeh Q, Fan LS, Warsito W. Electrical capacitance volume tomography: design and applications. *Sensors*. 2010;10:1890–1917.
28. Marashdeh QM, Tiexeria FL, Fan LS. Adaptive electrical capacitance volume tomography. *IEEE Sensors J*. 2014;14:1253–1259.
29. Verma V, Deen NG, Padding JT, Kuipers JAM. Two-fluid modeling of three-dimensional cylindrical gas–solid fluidized beds using the kinetic theory of granular flow. *Chem Eng Sci*. 2013;102:227–245.
30. van der Hoef MA, Beetstra R, Kuipers JAM. Lattice-Boltzmann simulations of low-Reynolds-number flow past mono- and bidisperse arrays of spheres: results for the permeability and drag force. *J Fluid Mech*. 2005;528:233–254.
31. Srivastava A, Sundaresan S. Analysis of a frictional-kinetic model for gas-particle flow. *Powder Technol*. 2003;129:72–85.
32. Roe PL. Characteristic-based schemes for the Euler equations. *Annu Rev Fluid Mech*. 1986;18:337–365.

Manuscript received May 4, 2015, and revision received July 8, 2015.